2D/3D Hybrid Cs$_2$AgBiBr$_6$ Double Perovskite Solar Cells: Improved Energy Level Alignment for Higher Contact-Selectivity and Large Open Circuit Voltage

Maximilian T. Sirtl, Rik Hooijer, Melina Armer, Firouzeh G. Ebadi, Mahdi Mohammadi, Clément Maheu, Andreas Weis, Bas T. van Gorkom, Sebastian Häringer, René A. J. Janssen, Thomas Mayer, Vladimir Dyakonov, Wolfgang Tress, and Thomas Bein*

Since their introduction in 2017, the efficiency of lead-free halide perovskite solar cells based on Cs$_2$AgBiBr$_6$ has not exceeded 3%. The limiting bottlenecks are attributed to a low electron diffusion length, self-trapping events and poor selectivity of the contacts, leading to large non-radiative V_{OC} losses. Here, 2D/3D hybrid double perovskites are introduced for the first time, using phenethyl ammonium as the constituting cation. The resulting solar cells show an increased efficiency of up to 2.5% for the champion cells and 2.03% on average, marking an improvement by 10% compared to the 3D reference on mesoporous TiO$_2$. The effect is mainly due to a V_{OC} improvement by up to 70 mV on average, yielding a maximum V_{OC} of 1.18 V using different concentrations of phenethylammonium bromide. While these are among the highest reported V_{OC} values for Cs$_2$AgBiBr$_6$ solar cells, the effect is attributed to a change in recombination behavior within the full device and a better selectivity at the interface toward the hole transporting material (HTM). This explanation is supported by voltage-dependent external quantum efficiency, as well as photoelectron spectroscopy, revealing a better energy level alignment and thus a better hole-extraction and improved electron blocking at the HTM interface.

1. Introduction

Halide double perovskites have recently attracted much interest in the photovoltaic community as they are seen as a possibility to solve several issues arising from their lead-based cousins featuring excellent optoelectronic properties.[1] Changing the simple perovskite ABX$_3$ structure to a 2 × 2 × 2 supercell, halide double perovskites have the general formula A$_2$B^{I}B^{III}X$_6$ where two bivalent cations B^{2+} are exchanged by a combination of one monovalent cation B$^+$ (e.g., Cu$^+$, Ag$^+$, Au$^+$, In$^+$) and one trivalent cation B^{3+} (e.g., Bi^{3+}, Sb^{3+}).[2] Several theoretical calculations have been performed on this structural motif, providing a large variety of proposed thermodynamically stable compounds of which Cs$_2$AgBiBr$_6$ proved to be the most promising material so far.[3–7] Cs$_2$AgBiBr$_6$ was characterized first by McClure et al.[8] and, being long-term stable at ambient conditions and providing alternative element combinations that exclude toxic elements,[2] this material was moved into the focus of research, especially due to promising optoelectronic properties of single crystals (for instance a charge carrier lifetime of >500 ns)[9,10] and the possibility to solution-process the material for thin films synthesis.[11]

After the first report on solar cells using Cs$_2$AgBiBr$_6$ as an active layer in 2017,[11] several groups reported solar cells

M. T. Sirtl, R. Hooijer, A. Weis, S. Häringer, T. Bein
Department of Chemistry and Center for NanoScience (CeNS)
University of Munich (LMU)
Butenandtstr. 11, 81377 Munich, Germany
E-mail: bein@lmu.de

M. Armer, V. Dyakonov
Experimental Physics VI
Julius Maximilian University of Würzburg
97074 Würzburg, Germany

The ORCID identification number(s) for the author(s) of this article can be found under https://doi.org/10.1002/aenm.202103215.

F. Ebadi, M. Mohammadi, W. Tress
Institute of Computational Physics (ICP)
ZHAW School of Engineering
Wildbachstr. 21, Winterthur 8400, Switzerland

C. Maheu, T. Mayer
Surface Science Laboratory
Department of Materials and Earth Sciences
Technical University of Darmstadt
Otto-Berndt-Strasse 3, 64287 Darmstadt, Germany

B. T. van Gorkom, R. A. J. Janssen
Molecular Materials and Nanosystems and Institute for Complex Molecular Systems
Eindhoven University of Technology
Eindhoven 5600 MB, Netherlands

implementing different architectures and contact layers. In order to optimize the optoelectronic properties and charge extraction behavior, the stoichiometric precursor ratio,[12,13] organic interface layers,[14] charge transport layers[15–18] and n-i-p, as well as p-i-n[19] structures have been investigated. Ultimately, these efforts led to power conversion efficiencies (PCE) that did not exceed 3.11% (or 4.23% using additional organic dyes) within several years of research.[16,20] Hence, present research activities aim at the investigation of the intrinsic bottlenecks of this material to find ways to overcome them and to push the solar cell efficiency further.

While the energy level alignment between the valence band maximum (VBM) of the double perovskite and the highest occupied molecular orbital (HOMO) energy level of the commonly used hole-transport materials (HTM) is non-optimal for solar cell functions,[15] the position of the conduction band minimum (CBM) leads to a low selectivity of the contacts within the full solar cell.[17] Moreover, a short electron diffusion length in deposited thin film structures,[21] ultra-fast self-trapping of free charge carriers[22] and large non-radiative V_{OC} losses have been found,[17] while it remains unclear whether a large exciton binding energy is hampering the solar cell efficiency[23,24] and how the PL signal of the thin films can be explained.[13,17,25]

Another challenge is the rather large and indirect bandgap of 1.9–2.3 eV,[13,26–28] especially since the stabilization of the related double perovskite Cs_2AgBiI_6 has not yet been realized due to the low thermodynamic stability of this compound.[29] While tuning of the absorption onset is pursued by using additives and alloying,[30–34] as well as high pressure modification,[35] a promising pathway to stabilize iodine based Ag-Bi double perovskites is the introduction of a large A-site cation in order to form 2D double perovskites, as first introduced by Connor et al. in 2018 using bromide.[36] Following this procedure, Jana et al. synthesized the first iodine based Ag-Bi double perovskite by using an oligothiophene based double cation 5,5′-diylbis(aminoethyl)-[2,2′-bithiophene] to stabilize $(AE2T)_2AgBiI_8$, which expressed a reduced and direct bandgap of 2 eV.[37] Going further, several other groups managed to stabilize the iodide phase using different spacer cations.[38,39] Due to the insulating properties of large organic cations, however, experience with lead-based perovskites shows a reduced efficiency of the pure 2D structures compared with their pure 3D counterpart.[40,41] To overcome this issue, either the formation of a quasi 2D perovskite ($n \geq 2$)

can be achieved by using small amounts of a small A^+ cation to partially substitute the large cation, or the formation of a hybrid perovskite can be pursued, using a 3D layer and combining it with a very thin 2D layer on top.[40,42–45]

In this work, we introduce the first 2D/3D hybrid double perovskite to date. By using the simple aromatic phenethyl ammonium bromide (PEABr) salt in 2-propanol, we show the formation of a $(PEA)_4AgBiBr_8$ layer on top of a 3D $Cs_2AgBiBr_6$ thin film. Moreover, we achieved the formation of a pure 2D $(PEA)_4AgBiBr_8$ thin film that shows excellent coverage and uniformity to determine the optical properties where we calculated the bandgap to be direct. Using an ultra-thin $(PEA)_4AgBiBr_8$ layer on top of the 3D film, we show that the efficiency of the resulting solar cell is boosted from 2.1% to 2.5%, which we assigned to a large increase of the V_{OC} and J_{SC} both for the champion cells and the cells showing average performance. Especially the V_{OC} values are the highest so far reported for this material, reaching up to 1.18 V. We assign these changes to an increase in the selectivity of the contacts, while the recombination behavior seems to remain the same, and support these findings with voltage dependent external quantum efficiency (EQE) measurements, as well as ultraviolet photoelectron spectroscopy (UPS), X-ray photoelectron spectroscopy (XPS) and photoluminescence measurements (PL). Overall, we show that utilizing 2D/3D hybrid double perovskites offers opportunities to address the issues regarding poor energy level alignment towards the HTM side and to easily fine-tune the contact-selectivity, ultimately boosting the overall solar cell efficiency.

2. Results and Discussion

2.1. Formation of the Hybrid Phase

In the field of 2D/3D hybrid perovskites, one approach to form such a layer is the deposition of the spacer cation on top of the already formed 3D film. This leads to the formation of a very thin 2D or 2D/3D hybrid top layer.[40,46] In our work, we adapted this approach and prepared the 3D layer first by spincoating the preheated $Cs_2AgBiBr_6$ stock solution on top of preheated glass substrates. This was followed by high temperature annealing (**Figure 1**). After the formation of the 3D film, we introduced the
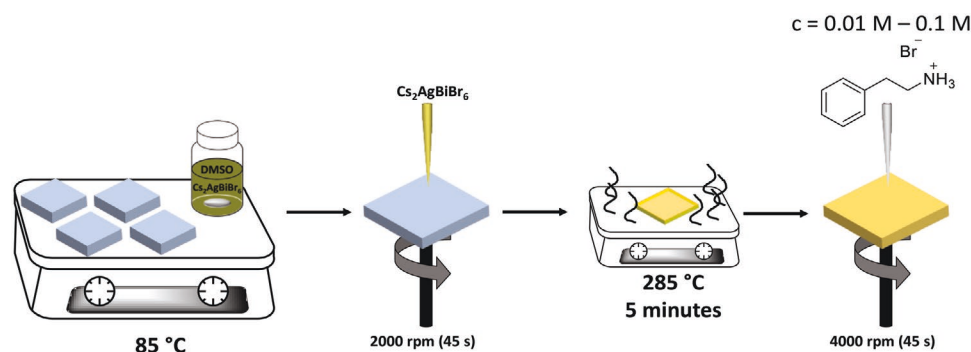

Figure 1. Schematic synthesis scheme for the 2D/3D hybrid double perovskite thin films. In a first step, we deposited the 3D double perovskite thin film by spincoating a preheated solution (85 °C) on a preheated substrate (85 °C) at 2000 rpm. After thermal annealing at 285 °C for 5 min, the spacer cation was spincoated on top of the 3D film at various concentrations (in IPA at 4000 rpm) to form a 2D/3D hybrid double perovskite film on top of the pure 3D layer. After addition of the spacer cation, no further annealing was applied.
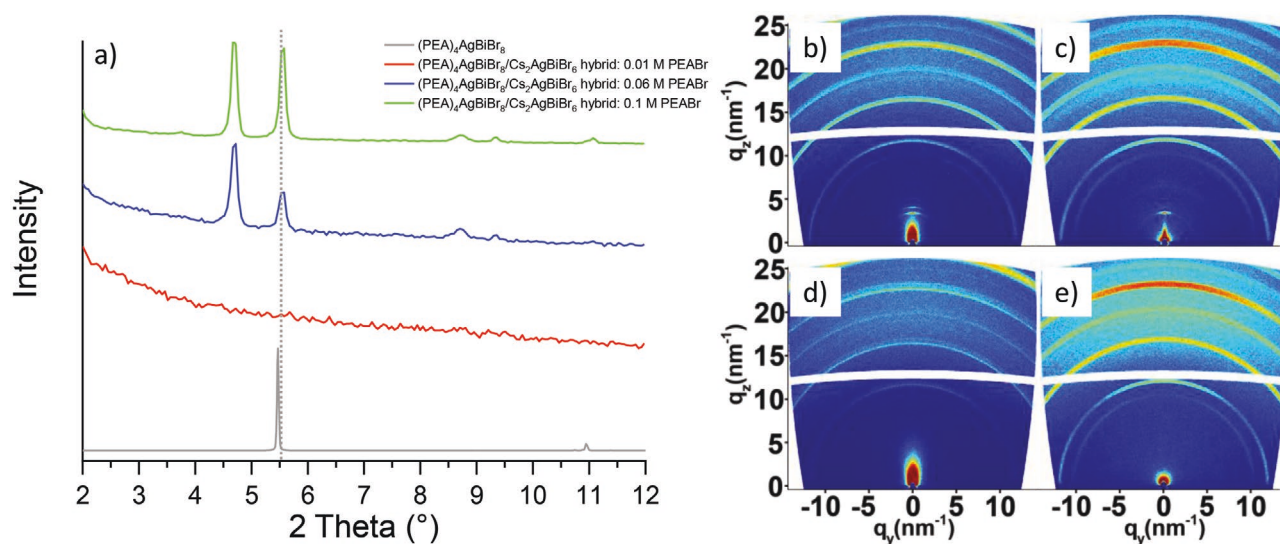
Figure 2. XRD pattern and GIWAXS data of the investigated thin films. a) Bragg-Brentano XRD patterns of modified thin films between 2 and 12° 2θ. Green (0.1 M PEABr), blue (0.06 M PEABr) and red lines (0.01 M PEABr) show the hybrid thin films while the grey line shows the theoretical pattern of the pure 2D $(PEA)_4AgBiBr_8$ double perovskite. The dashed grey line was added as a guide for the eye to emphasize the low-angle reflection. Panels (b)–(e) show the GIWAXS detector images of the b) 0.1 M, c) 0.06 M, and d) 0.01 M hybrid, as well as the e) 3D reference. The films were generated by spincoating the precursor solution on top of an FTO/c-TiO$_2$/mp-TiO$_2$ scaffold to simulate the same crystallization behavior utilized for the construction of solar cells.

spacer cation by spincoating phenethyl ammonium bromide (PEABr) on top, which is well known to form a 2D silver-bismuth perovskite phase.[47–49] We tested the hybrid perovskite formation with different PEABr concentrations in 2-propanol (*iso*propanol, IPA) ranging from 0.01 mol L^{-1} (0.01 M) to 0.1 M.

The insertion of long cations into a 3D perovskite leads to the formation of 2D phases with an increased lattice constant, which can be observed by the emergence of small angle XRD reflections.[36] To investigate the formation of a 2D layer on top of our 3D films, we performed both X-ray diffraction (XRD) in Bragg-Brentano geometry and grazing incidence wide angle X-ray scattering (GIWAXS) and compared the obtained patterns of the hybrid films (c(PEABr) = 0.1, 0.06, and 0.01 M) with the results for pure 3D films and the theoretical XRD pattern of the $n = 1$ $(PEA)_4AgBiBr_8$ structure (obtained from ref. [47]) as shown in **Figure 2** for the small angle region between 2 and 12° 2θ.

Figure 2a confirms the formation of the $(PEA)_4AgBiBr_8$ 2D-phase upon spincoating the spacer cation on top of the pure 3D films for PEABr concentrations ≥0.06 M. The comparison of the XRD pattern of the hybrid film with the calculated pattern of the pure 2D $(PEA)_4AgBiBr_8$ shows the formation of the characteristic reflection at low angles of 5.5° 2θ. However, the formation of this reflection cannot be observed using the lowest PEABr concentrations of 0.01 M. This suggests the formation of a rather thin 2D layer for low PEABr concentrations, which we confirmed through further GIWAXS measurements. Interestingly, one can see the formation of a second phase of the 2D perovskite at even smaller angles (≈4.5° 2θ). This can be related to the formation of 2D layers with n values bigger than one, which leads to a further increase of one unit cell dimension and hence to a shift of the reflection toward smaller angles. The full patterns in Figure S1, Supporting Information show that all

films are phase-pure with respect to undesired side phases such as AgBr, CsBr, or $BiBr_3$, as well as $Cs_3Bi_2Br_9$ and $(PEA)_3Bi_2Br_9$. The only additional reflections visible are gold-related peaks, which is expected as the XRD patterns were recorded on full solar cells.[50]

The GIWAXS measurements confirm the findings from the XRD measurements. Thin films treated with higher concentrated PEABr solutions (Figure 2b,c) show the formation of two peaks at low scattering vectors q compared to the 3D reference (Figure 2e), proving the presence of a low-dimensional phase. Using the same integration time, these reflections cannot be found for thin films treated with very low concentrated PEABr solutions (0.01 M, Figure 2d). However, by increasing the integration time by the factor 6, reflections at very small scattering vectors appear as shown in Figure S2, Supporting Information, demonstrating the formation of different 2D phases.

To further investigate the ultrathin 2D layers, SEM top-view images were recorded using the through-lens (TLD) and circular backscatter detector (CBS) as shown in the Supporting Information and **Figure 3**. The images compare the morphology of the above-discussed thin films with the 3D reference and the films obtained by spincoating PEABr solutions with the concentrations 0.1 and 0.01 M.

Figure 3 shows a zoom of the images shown in the Supporting Information. The morphology suggests the formation of rather big perovskite crystallites (>1 µm) that stick out from the mp-TiO$_2$ scaffold, which leads to rather large voids between the respective perovskite crystallites. However, this morphology has been proven to work well in solar cells[11] and the images clearly indicate the formation of a new layer for both PEABr concentrations. While the new layer forms big slabs within the voids of the 3D layer, the formation of this film can be seen
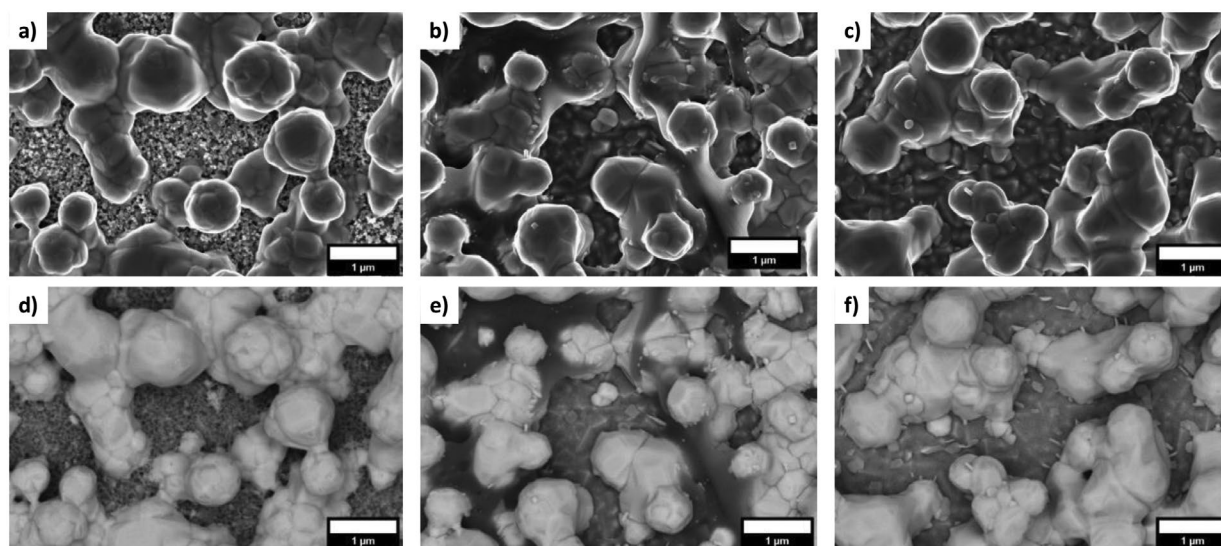
Figure 3. SEM top view images of the a,d) 3D reference, b,e) the 0.1 M hybrid, and c,f) the 0.01 M hybrid perovskite materials. The images (a)–(c) show the SEM top views obtained with a through-lens (TLD) and the images (d)–(f) show the images obtained with a circular backscatter detector (CBS). A smaller magnification can be found in the Supporting Information.

from the back-scatter images in Figure 3f) also for very low PEABr concentrations. Hence, we were able to confirm the formation of an additional low-dimensional double perovskite layer by spincoating a spacer cation on top of the 3D layer. We will now discuss the solar cells comprising this material as an active layer.

2.2. Solar Cell Performance

In the lead-halide perovskite community, it is well known that the hybridization of 3D films towards a 2D/3D structure can lead to an improvement of the photovoltaic performance of the resulting solar cells. This improvement has been attributed to better interfaces within the solar cells as well as trap passivation, resulting in a significant increase in V_{OC}.[42,45]

$Cs_2AgBiBr_6$ double perovskite solar cells, however, are known to suffer from a rather small electron diffusion length, a fast localization and self-trapping of charge carriers and, more importantly, from rather large non-radiative V_{OC} losses and non-selective contacts.[17,21,22]

To investigate the impact of the above discussed lead-free 2D/3D hybrid perovskite, we employed the thin films in solar cells with the architecture FTO/c-TiO$_2$/mp-TiO$_2$/Cs$_2$AgBiBr$_6$/(PEA)$_4$AgBiBr$_8$/Spiro-OMeTAD/Au. The results are shown in **Figure 4** and in **Table 1**. Please note that the PEABr concentrations of 0.01 and 0.06 M were chosen after a screening process, during which the thin films comprising these parameters were shown to improve the solar cells in comparison to other concentrations and the 3D reference. An exemplary J/V-curve of a 0.1 M device is shown in Figure S4, Supporting Information, where it is clearly seen that the PCE suffers from large J_{SC} losses as expected with a thicker 2D layer within the solar cell, hampering the charge transfer towards the back electrode. SEM cross-sections can be found in Figure S5, Supporting

Information, together with sketches of the layer-stacks of the investigated solar cells.

The values show a clear improvement of the solar cell efficiency by using 2D/3D hybrid perovskite active layers in the solar cells. The average results show an optimum cation concentration of 0.01 mol L^{-1} PEABr in IPA, as solar cells with this cation-concentration achieve the highest efficiencies, both in the champion and the average values. Solar cells made with 0.06 M PEABr do show a champion cell with 2.5% PCE as well, the average values though are lower compared to the 0.01 M cells.

For both 2D/3D hybrid double perovskite solar cells, maximum PCEs of up to 2.46% (0.01 M PEABr) and 2.47% (0.06 M PEABr) were achieved, which is an improvement of 13% compared to the 3D reference where the champion cell reached up to 2.15% PCE. J/V-curves of high-performance solar cells are shown in Figure S4, Supporting Information. While the high PCE of almost 2.5% is highly reproducible for the low concentrated (0.01 M PEABr, in the following called 0.01 M hybrid) hybrid, this value was only achieved once for the higher concentrated (0.06 M PEABr, in the following called 0.06 M hybrid) hybrid. This can be seen in the average values where the 3D reference results in 1.84% with 60 solar cells, while the 0.06 M hybrid shows an improvement to 1.95% with 68 devices. The 0.01 M hybrid double perovskite achieves also on average the highest PCE with 2.03%, which is almost 10% better compared to the 3D reference.

To find the reasons for the increase in efficiency, the different PV parameters need to be investigated. Figure 4 shows the different boxplots of the solar cells investigated in this work. While the fill factor only changes for the respective champion cells, it does not have an influence on the average improvement of the solar cells as it has values of 60% for both the 3D reference and the 0.01 M hybrid and only improves to 61% for the 0.06 M hybrid solar cells. The biggest changes in the photovoltaic (PV) parameters can be found in the open circuit voltage (V_{OC}) and the short circuit current (J_{SC}). For both parameters, an
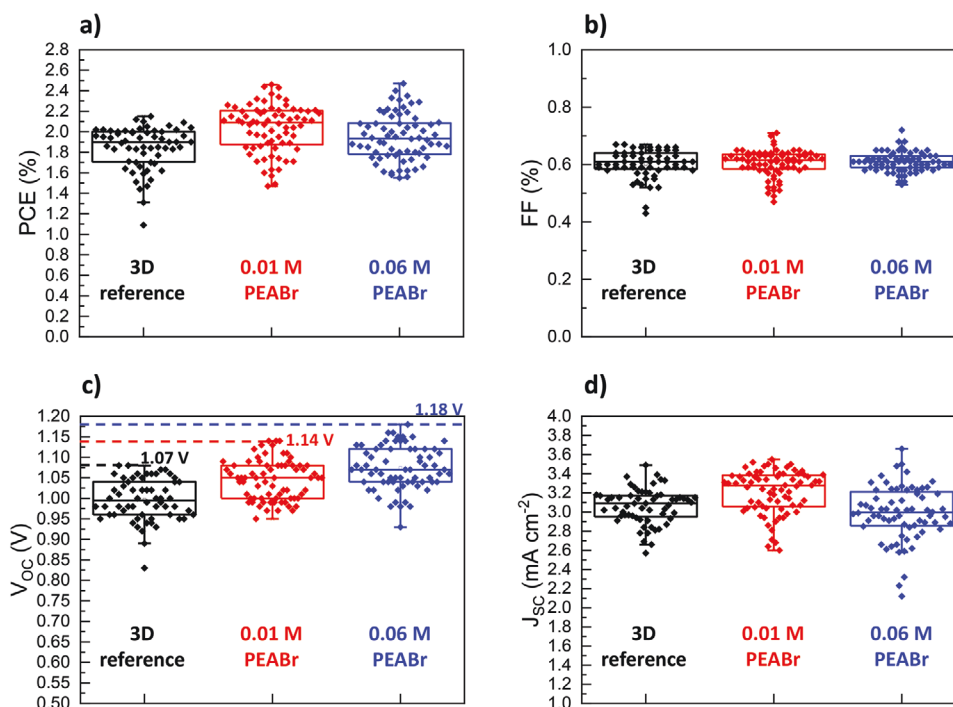
Figure 4. Box plots of the solar cell parameters of the investigated cells: black: 3D reference, red: 0.01 M hybrid, blue: 0.06 M hybrid. Panel (a) shows the power conversion efficiency (PCE) of the solar cells in %, panel (b) shows the fill factor (FF) of the solar cells, panel (c) shows the open circuit voltage (V_{OC}) in V and panel (d) shows the short circuit current (J_{SC}) in mA cm^{-2}. In panel (c), dashed horizontal lines were added as a guide to the eye to show the maximum achieved V_{OC} values in this work (color coded accordingly, the numbers show the actual values).

improvement is observed for the 0.01 M hybrid compared to the 3D reference, both for the champion device and the average of all devices. On average, the 0.01 M hybrid solar cells express an improvement in their V_{OC} by 60 mV from 0.99 to 1.05 V, which translates to 6%. For the 0.06 M hybrid, the V_{OC} improvement is even larger with 80 mV, leading to an average value of 1.07 V. For the J_{SC}, an improvement can only be found for the 0.01 M hybrid. Here, the average value increases by 5% from 3.06 mA cm^{-2} for the 3D reference to 3.21 mA cm^{-2} for the hybrid cell. For the 0.06 M hybrid, the average J_{SC} is reduced compared to the 3D reference with a value of 2.99 mA cm^{-2}. These effects are well within expectation and can be explained with the nature of the 2D perovskite. The addition of a 2D layer on top of a 3D layer is beneficial for the V_{OC} of the perovskite solar cells as already reported for lead-based perovskites.[40,42,45] Yet, a 2D layer is defined by its large organic cation, here a phenethyl ammonium cation. This leads to an insulating barrier on top of the 3D layer. While a thick 2D layer leads to a large improvement of the V_{OC}, it hampers charge transport from the 3D layer

towards the back electrode. The thinner this layer becomes, the more charge carriers can travel through this layer, hence the J_{SC} is improved. Another reason for the improvement of the J_{SC} can be found in the structure of the formed 2D perovskite: While for the 0.06 M hybrid, two phases with different n-values are formed, the only reflection found for the hybrids with concentrations of 0.01 M is for a phase with an n value >1. This translates to thicker octahedral layers in between the insulating PEA-layers and thus only a few insulating layers.

To further understand the improvement of the solar cells, additional measurements were performed.

2.3. Photoluminescence and Light Intensity Dependent V_{OC}

For lead-based 2D/3D hybrid perovskites, the corresponding reports discuss the improvement in the PCE and especially the V_{OC} with an increase in the signal of steady state photoluminescence, as well as an increase in the charge carrier lifetime obtained

Table 1. Photovoltaic parameters of the investigated solar cells with the architecture FTO/c-TiO$_2$/mp-TiO$_2$/perovskite/Spiro-OMeTAD/Au.

FTO/c-TiO$_2$/mp-TiO$_2$/perovskite/Spiro-OMeTAD/Au				
Perovskite [# of solar cells]	J_{SC} [mA cm^{-2}] [Avg]	V_{OC} [V] [Avg]	FF [%] [Avg]	PCE [%] [Avg]
pure 3D [60 devices]	3.33; [3.06 ± 0.18]	1.06; [0.99 ± 0.05]	60; [60 ± 5]	2.15; [1.84 ± 0.21]
2D/3D-hybrid, 0.06 M [68 devices]	3.50; [2.99 ± 0.28]	1.07; [1.07 ± 0.05]	66; [61 ± 3]	2.47; [1.95 ± 0.23]
2D/3D-hybrid, 0.01 M [72 devices]	3.55; [3.21 ± 0.22]	1.08; [1.05 ± 0.05]	64; [60 ± 5]	2.46; [2.03 ± 0.23]

**ADVANCED
SCIENCE NEWS**

www.advancedsciencenews.com

**ADVANCED
ENERGY
MATERIALS**
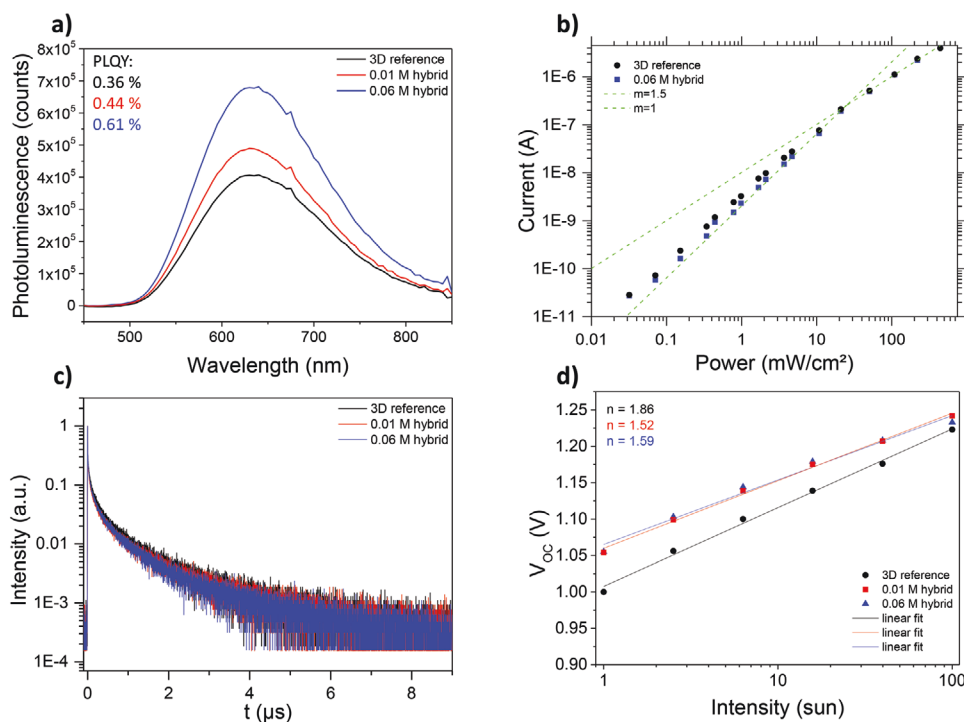
www.advenergymat.de

Figure 5. a) Steady state PL of the different films spincoated on glass, b) the fluence-dependent PL with m giving the slopes at different incident laser power, c) the PL decay of the different films. d) Shows the light intensity dependent V_{OC} measurements with the respective ideality factor given as n-value. All panels have the same color-coding: black: 3D reference, red: 0.01 M hybrid, blue: 0.06 M hybrid.

using time-resolved photoluminescence (TRPL).[40,42,45] Hence, we performed the same set of experiments as shown in **Figure 5**.

In contrast to lead-based perovskites, we did not observe any significant changes in the charge carrier behavior, both in the steady state and time resolved photoluminescence. This behavior is counter-intuitive, as we would expect a change in the recombination behavior of our thin films, especially the hybrids, following the V_{OC} trend from the solar cells. First, we measured the photoluminescence quantum yield (PLQY) of our thin films.

A small increase of the photoluminescence (PL) signal can be found (Figure 5a) for the 0.01 M hybrid, while the PL signal of the 0.06 M hybrid is almost double in intensity compared to the 3D film. To exclude measurement artifacts, every film was measured several times at several different spots. PLQY values show an improvement of the thin films from ≈0.36% for the 3D reference up to 0.61% for the 0.06 M hybrid, while the 0.01 M hybrid lies at around 0.44%. While all of these values are the highest so far reported for this material, they match well with the observed trend of the V_{OC} values of the solar cells.[21] Yet, the PLQY values are only sufficient to explain an increase of the V_{OC} by 20 mV in case of the 0.06 M hybrid films.[51] This shows that the dominant recombination regime might not change significantly, as no significant change in the radiative recombination yield was observed (as from the changes of V_{OC}, we would expect an increase of the signal by around two orders of magnitude). However, we do not claim that no passivation effect occurs at all. To investigate this further, we additionally measured fluence dependent steady state PL (Figure 5c) of the thin films on glass, comparing the 0.06 M hybrid with the 3D reference (as only for the 0.06 M hybrid, bigger changes are visible

so far). While the slopes in the fluence-dependent PL do change going from lower to higher laser intensity, this is expected from our previous work and can be explained as a shift from trap-assisted recombination towards excitonic recombination as at higher laser intensity, the ratio of free charge carriers to excitons is smaller compared to lower light intensity.[13,52] Among the different architectures, however, the data points do not show different values. This suggests that the dominating recombination behavior of the 2D/3D hybrid films is the same as for the 3D reference,[53] while all films have a change of the recombination regime going from low to high laser intensities (Figure 5b), which again indicates the formation of a hybrid phase instead of a simple passivation effect. Time resolved measurements (Figure 5c) do not show significant changes either, detecting a charge carrier lifetime of 331 ns for the 3D reference up to 352 ns for the 0.01 M hybrid and 356 ns for the 0.06 M hybrid, respectively. Hence, we can conclude that the lifetime of the charge carriers does not contribute significantly to the observed changes of the V_{OC}.

As an increased V_{OC} not only indicates changed recombination behavior in the pristine film, but can also be linked to better contact selectivity leading to a reduction of charge carrier recombination rates at the interface,[54,55] light intensity dependent V_{OC} measurements were performed as they are a valuable tool to determine the ideality factor of the diode that represents a solar cell. While fluence dependent steady state PL gives information about the recombination regime within the pristine film, the ideality factor does the same within the full device where n = 1 should indicate a perfect bimolecular recombination and n = 2 indicates a perfect trap assisted

recombination. The ideality factor can be deduced using the following Equation (1):[56]

$$V_{OC} \approx n \times \frac{kT}{e} \times \ln(I) \qquad (1)$$

where kT/e has a value of 0.02527 V at room temperature.

However, if the recombination behavior is dominated by interfacial recombination, the ideality factor may be equal to 1 as well and eventually reach values below 1.[56,57] In this case, the initial V_{OC} of the respective solar cell should be <1 V, which is not the case in this work.

Figure 5d shows the graphs obtained from measuring the three different solar cells, the values of the ideality factors obtained from the linear fit of the values in a ln plot (Figure S6, Supporting Information) are written in the figure. Contrary to the fluence-dependent PL measurements, the devices show in fact a change in the recombination behavior. While the 3D reference expresses an ideality factor of 1.86 at 395 nm excitation, indicating a mere trap assisted recombination behavior, the hybrid solar cells show values of 1.52 (0.01 M) and 1.59 (0.06 M), respectively. This could indicate a change of the recombination behavior towards both perfect bimolecular, or interfacial recombination.[56,57] As discussed above, however, a dominant interfacial recombination process would be associated with a rather low V_{OC} below 1 V. This is not the case in this work with average values of 1.07 and 1.05 V for 0.06 and 0.01 M cells respectively. Hence, the results indicate that for the 2D/3D hybrids, the recombination behavior is less dominated by interfacial and trap assisted recombination than compared to the 3D reference. This indicates a large improvement of the selectivity of the contacts, which we recently determined as one of the major bottlenecks.[17] The improvement of the charge carrier recombination in the full devices is further evidenced by EL EQE measurements that we performed using cells comprising the 3D reference and the 0.01 M hybrid solar cells. Here, an improvement of the EL EQE from 4×10^{-8} to 10^{-7} at the start of the measurement and from 1.5×10^{-8} to 10^{-7} after 170 s does show an increase of almost one order of magnitude for the 2D/3D hybrid solar cell (Figure S7, Supporting Information). While the value of the 3D reference is comparable to that from ref. [17], the 0.01 M cell indicates a significant improvement of the recombination behavior and thus explains a reduction of non-radiative V_{OC} losses (difference between radiative V_{OC} limit ($V_{OC,rad}$) and the V_{OC}) by up to 50 mV according to Equation (2):[17,27,28,58]

$$\Delta V_{OC} = V_{OC,rad} - V_{OC} = -\frac{kT}{q}\ln(EQE_{EL}) \qquad (2)$$

where kT/q is the thermal voltage.

Moreover, the measurement shows an improvement of the stability of the hybrid compared to the 3D reference. This is also evidenced by MPP tracking performed over a time-span of 3600 s. While both solar cells show a rather high stability of over 90%, the 0.01 M cell has an improved value of maintaining 99.6% of the initial PCE compared to the 3D reference (98.5%, Figure S7, Supporting Information).

To further investigate the origin of the higher selectivity and the improved J_{SC}, we proceeded with quantum efficiency measurements and band-energy determination.

2.4. PV Quantum Efficiency and Energy Level Alignment

The 0.06 M hybrid and the 0.01 M hybrid show very comparable behavior regarding the optoelectronic measurements, especially the light intensity dependent V_{OC} data. The 0.01 M films, however, show superior efficiency in solar cells, resulting from an improvement in both the J_{SC} and the V_{OC}. Hence, we will continue to discuss only the 0.01 M hybrid in the remainder of this paper.

Solar cells comprising the 0.01 M hybrid show an improved J_{SC} compared to the 3D reference (from 3.06 to 3.21 mA cm^{-2} on average). This can also be seen in the EQE spectra in **Figure 6**a. Here, the cells measured with the 0.01 M hybrid show a higher EQE compared to the 3D reference. Please note that we chose pixels (solar cell devices) for this measurement with a PCE well within the average of the solar cells described above. The biggest difference in the EQE is observable for the peak at ≈450 nm, where the absorption is the highest (dashed lines in Figure 6c,d). Here, the EQE is at 50% for the 2D/3D hybrid, while the EQE of the 3D reference only reaches 40%. Overall, an average increase of 10% in the EQE can be observed for the 2D/3D hybrid perovskite solar cells, which directly leads to an increased integrated photocurrent by almost 25% (2.3 to ≈2.9 mA cm^{-2}) which matches well with the obtained J_{SC} values from the solar cells (2.6 mA cm^{-2} for the 3D reference and 2.8 mA cm^{-2} for the hybrid). It confirms the trend visible from average values of all measured devices as shown in the section above. To further investigate the trap density and recombination behavior of the solar cells, subgap-EQE measurements were performed (Figure 6b). The spectra show no significant change in the trap density, observable by the signal in the spectral region below 2 eV. In fact, a slight increase in signal is observed for the 2D/3D hybrid double perovskite solar cells. This indicates that the hybrid cells express a slightly higher amount of gap-states and deep tails and confirms that no trap passivation occurred by hybridizing the 3D perovskite. It supports the finding that the boost in V_{OC} does not come from simple trap passivation.

In our recent publication, we observed a change of sign of the EQE by measuring the spectra as a function of the applied voltage, which was indicated by a large drop of the EQE at voltages >0.9 V.[17] While the bias causing this effect is much higher compared to our last work, we do see a very similar effect with the 3D solar cells: At voltages >1.00 V, we observe a drop in the EQE before it rises again strongly up to 80% (at 1.05 V external bias). The higher external voltage required compared to our recent report is well within the increase in the V_{OC} (0.9 V on average in ref. [17] compared to 0.99 V on average in the present work) and indicates either a larger built-in potential of 1 V that could be caused by the choice of Spiro-OMeTAD as HTM instead of P3HT. The first has a higher LUMO level compared to the latter, allowing for a better electron blocking and therefore a better overall selectivity.[59] In the present work, we again observe not only an increase of the absolute EQE values, but also a change in the shape. While the shape of the EQE spectra below 1 V external bias exactly follows the absorption peaks of the UV–vis spectrum (grey dashed line in Figure 6c), this shape is inverted after applying voltages above 1.00 V. Now, the EQE maxima are located at the spectral range of the
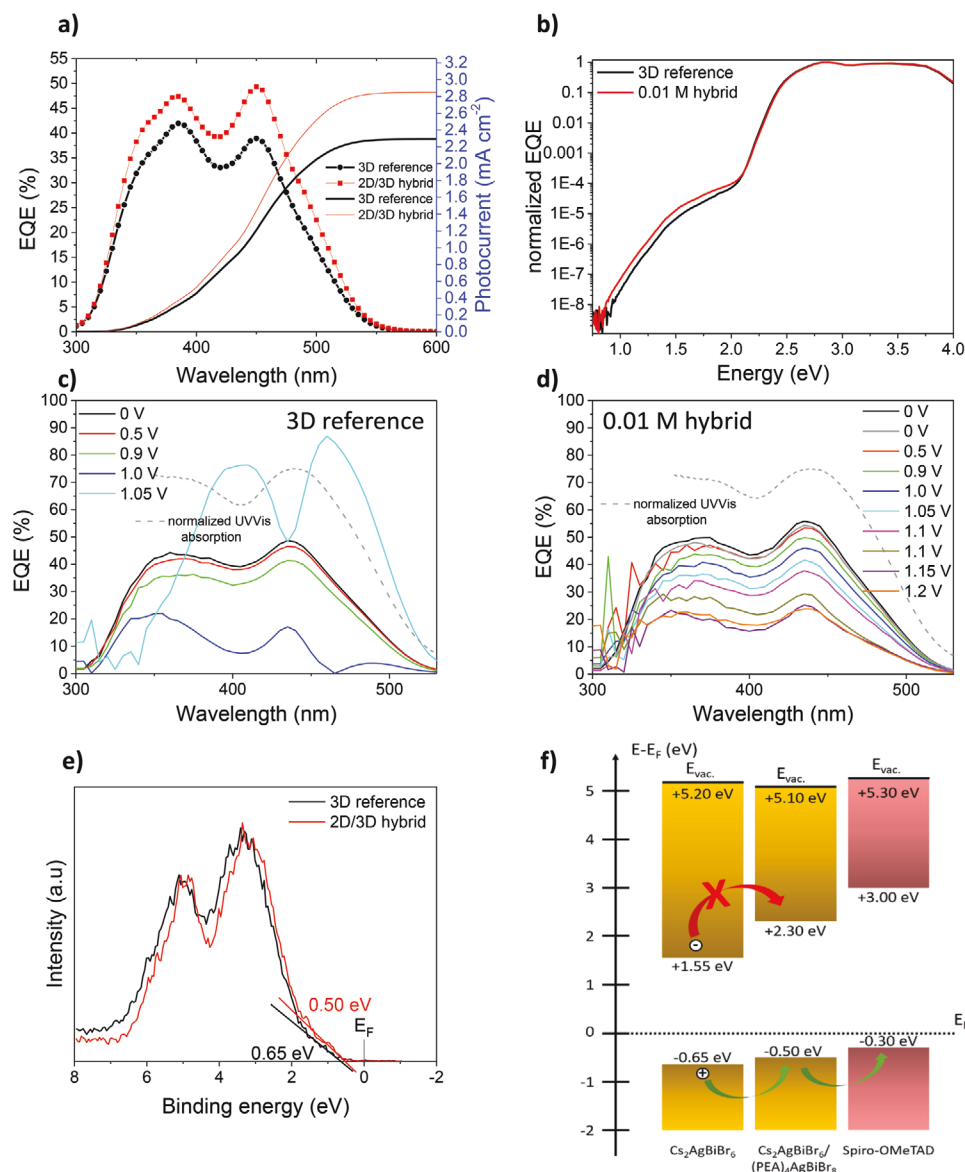
Figure 6. EQE and XPS spectra measured in this work. a) The EQE spectra obtained from the 3D reference (red line) and the 0.01 M hybrid (black line), plotted together with the integrated photocurrent. Panel (b) shows the subgap EQE spectra of the 3D reference (red line) and the 0.01 M hybrid (black line). Panels (c) and (d) show the voltage-dependent EQE measurements of the 3D reference and the 0.01 M hybrid, respectively. Different applied voltages are shown in the legend. The dashed grey line shows the respective UV–vis absorption spectrum to guide the eye. Panel (e) shows the XPS spectra of the valence shell energies of the hybrid double perovskite (red line) with respect to the 3D reference (black line). Panel (f) shows a schematic energy level diagram obtained from the XPS values of the VBM and the optical bandgap obtained from the Tauc plots in the Supporting Information.

absorption minima, which indicates that the charge carriers created more homogeneously in the perovskite layer result in a higher photocurrent. The high EQE value can only be explained by a photomultiplication effect due to a photoenhanced forward current. Given the well-aligned conduction band of TiO_2 and perovskites, this current is most likely carried by electrons, which recombine with holes on the HTM. This further confirms the findings of our recent work that we indeed have rather non-selective contacts and thus reduce the charge carrier collection.[17]

For the 2D/3D hybrid perovskite, no such change in the EQE is observed, at least for voltages up to 1.20 V. Here, the values of

the EQE steadily decrease, as also observed for the 3D reference. Upon reaching voltages >1.25 V, the solar cell rapidly degrades and the measured values are not reliable. To make sure that the trend below 1.25 V is reproducible, we remeasured the EQE at 0 and 1.1 V and observed only slight changes in the EQE. The absence of the photocurrent inversion for the 2D/3D hybrid double perovskite solar cells indicates a large improvement of the selectivity within the solar cell, as not only the V_{OC} of the solar cell is increased (indicating an even larger internal voltage, as well as built-in potential), but also the photocurrent direction shows no change at all, indicating a higher selectivity of the contacts. These results, together with the absence of trap passivation,

support the indications of an increased contact selectivity, as well as reduced interface recombination leading to the significant improvement of the V_{OC} values of the resulting solar cells as observed with light intensity-dependent V_{OC} measurements.

To investigate the energy levels, photoelectron spectroscopy measurements were performed on the perovskites deposited on FTO substrates as shown in Figure 6e, Figures S7 and S8, Supporting Information.

Since the films were deposited at ambient conditions in air, contamination with oxygen could not be excluded. Hence, not UV irradiation but X-rays were used to determine the valence band maxima of the two different films. To confirm the presence of the spacer cation for the 2D/3D hybrid thin films, we determined the core-level energies of the different samples. Figure S9, Supporting Information exhibits the survey and the core level XPS spectra for the 3D reference and a 2D/3D hybrid. Binding energy positions of each element agree with a previous report.[12] The presence of nitrogen in the 2D/3D hybrid thin film confirms the presence of the spacer cation. A narrowing of the core level emission lines is also observed when the spacer cation is added. On average, the FWHM decreases to 100 meV and for the Br 3d spectra, it leads to more defined emission lines. This is in agreement with an ordering of the perovskite after a 3D to 2D transition[47,48] and confirms the presence of a 2D/3D hybrid phase. The nitrogen spectrum (N1s) can only be found for the 2D/3D hybrid material. However, the Cs 3d emission lines are visible as well, indicating that the contribution of the 3D phase to the PES spectra cannot be dismissed. This can be linked to the morphology of the investigated thin films as shown in Figure 3 and Figure S3, Supporting Information, showing the μm-sized 3D perovskite crystallite penetration out of the 2D layer.

Figure 6e shows a shift of the VBM after the addition of a spacer cation. It establishes that the VBM of the 2D material is 150 meV closer to the Fermi level, compared to the 3D reference. This is supported by the similar shifts of 100 meV (Bi4f, Ag3d) or 150 meV (Br3d, Cs3d) that are observed on the core level emission lines (Figure S9, Supporting Information). As all measurements are performed relative to the Fermi level of the sample, such global shift toward lower energy indicates a change in the Fermi level position of the perovskite absorber.

To determine the energy of the conduction band minimum, we measured the optical bandgap of a pure 2D (PEA)$_4$AgBiBr$_8$ thin film (Figure S11, Supporting Information). The thin film was deposited on an FTO substrate to simulate the same environment as for the 3D thin films, resulting in fully covered, smooth thin films (inset in Figure S11a, Supporting Information). To determine the nature of the optical bandgap of the material, we calculated the band structure using first principle DFT calculations (Figure S12, Supporting Information). The PBE-SOC-TS band structure of (PEA)$_4$AgBiBr$_8$ shows a drastic change in the nature of the band gap compared to the 3D reference perovskite with the lowest band transition being centered at the Γ point in the Brillouin zone.[36] We note that although the bandgap is significantly underestimated, we can assume that the DFT-PBE method provides accurate predictions about the electronic nature of the calculated structure.[60,61] Hence, a direct bandgap with an energy of 2.8 eV was obtained (Figure S11,

Supporting Information), increasing the energy by 0.6 eV compared to the 3D Cs$_2$AgBiBr$_6$.[17]

Combining the optical bandgap, the VBM and the work function measured by UPS (Figure S10, Supporting Information), the full band diagram can be constructed (Figure 6f). To provide more insight on the charge carrier collection of our device, the energy levels of the HTM, a LiTFSI-doped Spiro-OMeTAD, were determined and added to the diagram. The corresponding VBM and the work function were measured with UPS (Figure S11, Supporting Information) and the band gap was assumed to be 3.3 eV, although the absorption energy of the oxidized species is slightly lower.[62] The 2D perovskite has a CBM of +2.3 eV (relatively to the Fermi level) which is 750 meV above the one of the 3D counterpart and 700 meV below the LUMO of the HTM. As the electrons are photogenerated inside the 3D material, the presence of the 2D layer enhances the electron blocking behavior of the resulting hybrid thin films. In addition, the VBM of the 2D/3D hybrid double perovskite is 150 meV closer to the HOMO energy level of the HTM compared to the 3D reference. It optimizes the holes extraction and therefore, it reduces the amount of interfacial recombination.

This altogether confirms the findings of the EQE measurements that indicate a significant change in the selectivity of the contacts in the solar cell. It leads to the observed boost in the V_{OC} of the solar cells and addresses one of the major issues of solar cells based on Pb-free perovskites.

3. Conclusions

In this work, we successfully synthesized an Ag-Bi based 2D/3D hybrid double perovskite for the first time, using phenethyl ammonium bromide as large cation salt to form Cs$_2$AgBiBr$_6$/(PEA)$_4$AgBiBr$_8$ thin films. After confirmation of the film formation, we implemented this material in perovskite solar cells, obtaining a significant increase in the PCE from 1.84% on average for the 3D reference to 2.03% for the 2D/3D hybrid. The champion cells comprising the 2D/3D hybrid thin film even reach efficiencies of up to 2.5%. While the J_{SC} shows an improvement of 10% on average, the V_{OC} is improved on average by 70 mV to reach values of up to 1.14 and 1.18 V, which are among the highest values reported for Cs$_2$AgBiBr$_6$ solar cells. This boost in the V_{OC} is attributed to a large enhancement of the selectivity of the contacts in the solar cell, which was shown by comprehensive EQE and PL studies. Photoelectron spectroscopy reveals a shift in the valence band maximum of the 2D/3D hybrid perovskite thin film of 150 meV toward the Fermi level energy. This improves the energy level alignment and allows for a better hole-extraction towards the doped Spiro-OMeTAD layer. In combination with an increased bandgap of the 2D material, which was calculated to be direct, the XPS results predict an energy barrier of 750 meV between the 2D and the 3D perovskite, improving the contact selectivity in the solar cell. In this work, we show a way to easily tune the perovskite/HTM energy level alignment, as well as to improve the charge carrier selectivity of the contacts in the solar cell. Hence, this work offers a toolbox to efficiently address some of the bottlenecks that have been identified for the behavior of lead-free double perovskite solar cells.

4. Experimental Section

Materials and Thin Film synthesis: The stock solution was prepared by dissolving CsBr (Alpha Aesar, 99.999% metals basis), BiBr₃ (Alpha Aesar, 99.9% metals basis) and AgBr (Alpha Aesar, 99.998% metals basis) in 1 mL DMSO (Sigma Aldrich, anhydrous, ≥99.9%) by vigorous stirring at 130 °C for 60 min to obtain a 0.5 M solution. Weighing the precursors was performed in a nitrogen-filled glovebox, while all other steps, including the DMSO addition to the precursors, were done at ambient conditions in air.

Prior to the spincoating step, the substrates and the solution were placed on a hotplate (Heidolph with internal temperature sensor) at 85 °C to be preheated. The stock solution was constantly stirred. The thin films were fabricated by spincoating the warm solution dynamically (2000 rpm for 45 s) onto the preheated substrates (100 µL of the stock solution). After the spincoating, the thin films were annealed at 285 °C for 5 min at ambient conditions in air.

Solar Cell Fabrication: Fluorine-doped tin oxide coated glass sheets (7 Ω sq⁻¹) were patterned by etching with zinc-powder and 3 M HCl, cleaned with a detergent followed by washing with acetone and ethanol and dried under an air stream. Directly before applying the hole-blocking layer, the substrates were oxygen plasma cleaned for 5 min.

Compact TiO₂ (c-TiO₂): A compact TiO₂ layer was prepared from a sol-gel precursor solution by spin-coating 100 µL onto the 3 cm × 3 cm substrates for 45 s at 2000 rpm and calcination afterwards at 500 °C for 30 min in air, resulting in a 50 nm thick layer. For the sol-gel solution, 2 M HCl (35 µL) in 2.53 mL dry 2-propanol was added dropwise to a solution of 370 µL of titanium-isopropoxide in 2.53 mL dry 2-propanol under vigorous stirring. After cooling down, the substrates were again plasma cleaned for 5 min and transferred to a nitrogen-filled glovebox.

Mesoporous TiO₂ (mp-TiO₂): After the deposition of the layer of compact TiO₂, 100 µL of a dispersion of mp-TiO₂ nanoparticles (DyeSol, 3:1 EtOH:TiO₂-paste) was spincoated on top of the c-TiO₂ layer without plasma-cleaning. Afterward, the substrates were calcined at 500 °C for 30 min in air resulting in a 500 nm thick layer. After cooling down, the active layer was deposited on top of the TiO₂ layer as described above.

Deposition of Hole Transporting Materials (HTM): 73 mg of 2,2′,7,7′-tetrakis-(*N*,*N*-di-4-methoxyphenylamino)-9,9′-spirobifluorene (Spiro-OMeTAD, Borun Chemicals, 99.5% purity) were dissolved in 1 mL of chlorobenzene. To this solution, 10 µL of 4-tert-butylpyridine and 30 µL of a bis(trifluoromethane)sulfonamide lithium salt solution (LiTFSI, 170 mg in 1 mL acetonitrile) were added. The resulting HTM solution was deposited via dynamic spincoating (1500 rpm, 45 s) in a nitrogen-filled glovebox. Afterward, the samples were stored overnight in air at <30% relative humidity (R.H.) to allow the hole transporting material to oxidize.

The top electrode with a thickness of 40 nm was deposited by thermally evaporating gold under vacuum (at ≈10⁻⁷ mbar).

DFT Calculations: First-principle DFT calculations were based on a plane wave basis set and norm-conserving Vanderbilt pseudopotentials as implemented in the Quantum Espresso package.[63,64] Furthermore, the PBE exchange–correlation functional and the Tkatchenko–Scheffler (TS) dispersion scheme were used.[65,66] The latter is necessary to accurately describe the structural properties in low-dimensional perovskite materials.[67] Additionally, spin-orbit coupling was included to treat the heavy Bi atom. The structure, starting from the single crystal data of Schmitz et al.,[49] was optimized until all residual forces on the nuclei were below 1.0×10^{-3} a.u. Thereby, the following equilibrium unit cell parameters were obtained:

$a = 11.4661$ Å, $b = 11.5138$ Å, $c = 17.0237$ Å, $\alpha = 106.6141°$, $\beta = 99.6955°$, $\gamma = 90.7676°$

A kinetic energy cutoff of 50 Ry for the wavefunctions and 400 Ry for the charge density was used. A $4 \times 4 \times 1$ k-point grid was utilized.

Materials Characterization: *Powder X-Ray Diffraction (PXRD) Measurements*: The patterns were recorded using a Bruker D8 Discover Diffractometer with Ni-filtered Cu K_α radiation and a LynxEye position-sensitive detector.

2D Grazing-incidence wide angle X-ray scattering (GIWAXS): GIWAXS measurements were carried out on a ANTON-PAAR SAXSPOINT 2.0 with a Primux 100 microfocus source with Cu-$K_{\alpha 1}$ radiation ($\lambda = 1.5406$ Å) and a DECTRIS EIGER R 1M 2D Detector.

Scanning Electron Microscopy (SEM): SEM data were taken with an FEI Helios NanoLab G3 UC field emission scanning electron microscope equipped with an additional concentric backscattered electron detector.

Photoelectron Spectroscopy (PES): Even though the samples were prepared under ambient conditions in air, to minimize contaminations, samples were shipped under nitrogen. They were opened in a glovebox and transferred to the ultra high vacuum system.

PES measurements were performed with a Thermo Fisher VG Escalab 250 spectrometer. It was equipped with a monochromatic X-ray source (Al Kα = 1486.6 eV) set at 13 mA and 15 kV. The pressure inside the analytical chamber was monitored below 5×10^{-9} mbar. Measurements were performed in "dark conditions" as discussed in ref. [68] to avoid undesired photovoltage and misinterpretation of the energy levels.

Survey spectra were acquired with a pass energy of 50 eV, a step size of 0.1 eV and a dwell time of 50 ms per measurement point. The detailed scans were acquired with a lower pass energy (10 eV) and a lower step size (0.05 eV). UPS measurements were performed with the same spectrometer; He I (21.2 eV) discharge was used.

XPS spectra were calibrated using the Fermi level of silver (0 eV) measured by XPS as well as the binding energy of the Au 4f$_{7/2}$ emission line (84.0 eV), the Ag 3d$_{5/2}$ emission line (368.26 eV – FWHM at a pass energy of 10 eV was equal to 0.52 eV), and the Cu 2p$_{3/2}$ emission line (932.67 eV). The Femi level of silver was also measured with UPS to calibrate the corresponding spectra. The Fermi level value was determined with a sigmoid fit and taking the position where the intensity is at 50%. All calibration samples were cleaned with Ar sputtering prior to the measurement (3 kV, for 180 s). The Fermi level of the cleaned silver was also used to determine the instrumental resolution: 0.35 eV for XPS (pass energy of 10 eV) and 0.24 eV for UPS (pass energy of 2.5 eV).

Semi quantitative analysis was performed using the Thermo Avantage software. Core levels were fitted using modified Shirley background subtraction and Gauss-Lorentz convolution. Quantification was made with the machine-corrected atomic sensitivity factors based on Scofield's calculations.

Photoluminescence Quantum Yield (PLQY), Fluence Dependent Steady State PL and Time-correlated Single Photon Counting (TCSPC): The PLQY was measured using a laser with 405 nm wavelength, a power of 71.0 mW cm⁻² and an integrating sphere. The spot size was 0.0152 cm².

The TRPL was recorded using a 375 nm laser with a repetition rate of 10 µs, an energy density of 8.3 nJ cm⁻² and a spot size of 290 µm.

All spectra were measured using an Edinburgh Instruments FLS 980 spectrometer in reflection using a Si diode for detection.

Fluence-dependent steady state PL was measured using a 415 nm LED (Solis-415C, Thorlabs). The sample was placed at a 45° angle toward the excitation beam, so that measurements were performed in a reflection configuration. A silicon diode was placed in the emission pathway in order to monitor the resulting integrated photoluminescence.

EQE Measurements for Figure 6: Measurements were performed on a homemade system with a halogen lamp, a monochromator and a silicon reference diode. The light was chopped at 330 Hz and the signal was detected through a lock-in amplifier. The setup was calibrated with a silicon solar cell and no bias light was applied.

Sensitive EQE Measurements: Sensitive EQE measurements to characterize the sub-bandgap region were conducted using a halogen lamp (Osram 64 655 HLX 250 W) as illumination source. The light was chopped using an Oriel 3502 chopper at 330 Hz and subsequently passed through a double-grating monochromator (Oriel, Cornerstone 260). Several long-pass filters were used to filter out stray light. The samples were mounted in an air tight holder filled with nitrogen to prevent air exposure. The response was recorded from a pre-amplifier (Stanford Research, SR 570) using a lock-in amplifier (Stanford Research, SR 830) and calibrated using two Si and InGaAs reference cells.

Absorption Measurements: The absorption spectra of the films were taken on a Lambda 1050 (Perkin Elmer) instrument with an integrating sphere.

**ADVANCED
SCIENCE NEWS**

www.advancedsciencenews.com

**ADVANCED
ENERGY
MATERIALS**

www.advenergymat.de

Solar Cell characterization: Current–voltage (*J–V*) characteristics of the perovskite solar cells were measured using a Newport OrielSol 2A solar simulator with a Keithley 2401 source meter. The devices were illuminated through a shadow mask, yielding an active area of 0.0831 cm^2. The *J–V* curves were recorded under standard AM 1.5G illumination from a xenon lamp, and calibrated to a light intensity of 100 mW cm^{-2} with a Fraunhofer ISE certified silicon diode. The input bias voltage was scanned from −1.5 to 0 V in 0.01 V steps with a rate of 0.1 V s^{-1} for the standard PCE measurements. For the experiments with different scan-speeds, bigger voltage steps varying from 0.01 to 1 V were chosen. All prepared devices show a comparable degree of hysteresis between the forward and the reverse scan.

Supporting Information

Supporting Information is available from the Wiley Online Library or from the author.

Conflict of Interest

The authors declare no conflict of interest.

Data Availability Statement

The data that support the findings of this study are available in the supplementary material of this article.

[1] M. Green, E. Dunlop, J. Hohl-Ebinger, M. Yoshita, N. Kopidakis, X. Hao, *Prog. Photovolt. Res. Appl.* **2021**, *29*, 3.

[2] X.-G. Zhao, J.-H. Yang, Y. Fu, D. Yang, Q. Xu, L. Yu, S.-H. Wei, L. Zhang, *J. Am. Chem. Soc.* **2017**, *139*, 2630.

[3] Z. Xiao, W. Meng, J. Wang, Y. Yan, *ChemSusChem* **2016**, *9*, 2628.

[4] M. R. Filip, X. Liu, A. Miglio, G. Hautier, F. Giustino, *J. Phys. Chem. C* **2018**, *122*, 158.

[5] G. Volonakis, M. R. Filip, A. A. Haghighirad, N. Sakai, B. Wenger, H. J. Snaith, F. Giustino, *J. Phys. Chem. Lett.* **2016**, *7*, 1254.

[6] M. R. Filip, S. Hillman, A. A. Haghighirad, H. J. Snaith, F. Giustino, *J. Phys. Chem. Lett.* **2016**, *7*, 2579.

[7] G. Volonakis, A. A. Haghighirad, H. J. Snaith, F. Giustino, *J. Phys. Chem. Lett.* **2017**, *8*, 3917.

[8] E. T. McClure, M. R. Ball, W. Windl, P. M. Woodward, *Chem. Mater.* **2016**, *28*, 1348.

[9] A. H. Slavney, T. Hu, A. M. Lindenberg, H. I. Karunadasa, *J. Am. Chem. Soc.* **2016**, *138*, 2138.

[10] R. L. Z. Hoye, L. Eyre, F. Wei, F. Brivio, A. Sadhanala, S. Sun, W. Li, K. H. L. Zhang, J. L. MacManus-Driscoll, P. D. Bristowe, R. H. Friend, A. K. Cheetham, F. Deschler, *Adv. Mater. Interfaces* **2018**, *5*, 1800464.

[11] E. Greul, M. L. Petrus, A. Binek, P. Docampo, T. Bein, *J. Mater. Chem. A* **2017**, *5*, 19972.

[12] F. Igbari, R. Wang, Z.-K. Wang, X.-J. Ma, Q. Wang, K.-L. Wang, Y. Zhang, L.-S. Liao, Y. Yang, *Nano Lett.* **2019**, *19*, 2066.

[13] M. T. Sirtl, M. Armer, L. K. Reb, R. Hooijer, P. Dörflinger, M. A. Scheel, K. Tvingstedt, P. Rieder, N. Glück, P. Pandit, S. V. Roth, P. Müller-Buschbaum, V. Dyakonov, T. Bein, *ACS Appl. Energy Mater.* **2020**, *3*, 11597.

[14] X. Yang, Y. Chen, P. Liu, H. Xiang, W. Wang, R. Ran, W. Zhou, Z. Shao, *Adv. Funct. Mater.* **2020**, *30*, 2001557.

[15] B. Wang, L. Yang, C. Dall'Agnese, A. K. Jena, S.-I. Sasaki, T. Miyasaka, H. Tamiaki, X.-F. Wang, *Sol. RRL* **2020**, *4*, 2000166.

[16] B. Wang, N. Li, L. Yang, C. Dall'Agnese, A. K. Jena, S.-I. Sasaki, T. Miyasaka, H. Tamiaki, X.-F. Wang, *J. Am. Chem. Soc.* **2021**, *143*, 2207.

[17] M. T. Sirtl, F. Ebadi, B. T. Gorkom, P. Ganswindt, R. A. J. Janssen, T. Bein, W. Tress, *Adv. Optical Mater.* **2021**, *9*, 2100202.

[18] C. Wu, Q. Zhang, Y. Liu, W. Luo, X. Guo, Z. Huang, H. Ting, W. Sun, X. Zhong, S. Wei, S. Wang, Z. Chen, L. Xiao, *Adv. Sci.* **2018**, *5*, 1700759.

[19] W. Gao, C. Ran, J. Xi, B. Jiao, W. Zhang, M. Wu, X. Hou, Z. Wu, *ChemPhysChem* **2018**, *19*, 1696.

[20] B. Wang, N. Li, L. Yang, C. Dall'Agnese, A. K. Jena, T. Miyasaka, X.-F. Wang, *J. Am. Chem. Soc.* **2021**, *143*, 14877.

[21] G. Longo, S. Mahesh, L. R. V. Buizza, A. D. Wright, A. J. Ramadan, M. Abdi-Jalebi, P. K. Nayak, L. M. Herz, H. J. Snaith, *ACS Energy Lett.* **2020**, *5*, 2200.

[22] A. D. Wright, L. R. V. Buizza, K. J. Savill, G. Longo, H. J. Snaith, M. B. Johnston, L. M. Herz, *J. Phys. Chem. Lett.* **2021**, *12*, 3352.

[23] D. Bartesaghi, A. H. Slavney, M. C. Gélvez-Rueda, B. A. Connor, F. C. Grozema, H. I. Karunadasa, T. J. Savenije, *J. Phys. Chem. C* **2018**, *122*, 4809.

[24] R. Kentsch, M. Scholz, J. Horn, D. Schlettwein, K. Oum, T. Lenzer, *J. Phys. Chem. C* **2018**, *122*, 25940.

[25] S. J. Zelewski, J. M. Urban, A. Surrente, D. K. Maude, A. Kuc, L. Schade, R. D. Johnson, M. Dollmann, P. K. Nayak, H. J. Snaith, P. Radaelli, R. Kudrawiec, R. J. Nicholas, P. Plochocka, M. Baranowski, *J. Mater. Chem. C* **2019**, *7*, 8350.

[26] M. Armer, J. Höcker, C. Büchner, S. Häfele, P. Dörflinger, M. T. Sirtl, K. Tvingstedt, T. Bein, V. Dyakonov, *CrystEngComm* **2021**, *23*, 6848.

[27] H. Lei, D. Hardy, F. Gao, *Adv. Funct. Mater.* **2021**, *31*, 2105898.

[28] W. Tress, M. Sirtl, *Sol. RRL*, https://doi.org/10.1002/solr.202100770.

[29] P. Vishnoi, R. Seshadri, A. K. Cheetham, *J. Phys. Chem. C* **2021**, *125*, 11756.

[30] N. Pai, J. Lu, M. Wang, A. S. R. Chesman, A. Seeber, P. V. Cherepanov, D. C. Senevirathna, T. R. Gengenbach, N. V. Medhekar, P. C. Andrews, U. Bach, A. N. Simonov, *J. Mater. Chem. A* **2020**, *8*, 2008.

[31] Z. Li, S. R. Kavanagh, M. Napari, R. G. Palgrave, M. Abdi-Jalebi, Z. Andaji-Garmaroudi, D. W. Davies, M. Laitinen, J. Julin, M. A. Isaacs, R. H. Friend, D. O. Scanlon, A. Walsh, R. L. Z. Hoye, *J. Mater. Chem. A* **2020**, *8*, 21780.

[32] F. Ji, J. Klarbring, F. Wang, W. Ning, L. Wang, C. Yin, J. S. M. Figueroa, C. K. Christensen, M. Etter, T. Ederth, L. Sun, S. I. Simak, I. A. Abrikosov, F. Gao, *Angew. Chem., Int. Ed.* **2020**, *132*, 15303.

[33] E. M. Hutter, M. C. Gélvez-Rueda, D. Bartesaghi, F. C. Grozema, T. J. Savenije, *ACS Omega* **2018**, *3*, 11655.

ADVANCED
SCIENCE NEWS
www.advancedsciencenews.com

ADVANCED
ENERGY
MATERIALS
www.advenergymat.de

[34] A. Karmakar, M. S. Dodd, S. Agnihotri, E. Ravera, V. K. Michaelis, *Chem. Mater.* **2018**, *30*, 8280.

[35] Q. Li, Y. Wang, W. Pan, W. Yang, B. Zou, J. Tang, Z. Quan, *Angew. Chem., Int. Ed.* **2017**, *56*, 15969.

[36] B. A. Connor, L. Leppert, M. D. Smith, J. B. Neaton, H. I. Karunadasa, *J. Am. Chem. Soc.* **2018**, *140*, 5235.

[37] M. K. Jana, S. M. Janke, D. J. Dirkes, S. Dovletgeldi, C. Liu, X. Qin, K. Gundogdu, W. You, V. Blum, D. B. Mitzi, *J. Am. Chem. Soc.* **2019**, *141*, 7955.

[38] L.-Y. Bi, Y.-Q. Hu, M.-Q. Li, T.-L. Hu, H.-L. Zhang, X.-T. Yin, W.-X. Que, M. S. Lassoued, Y.-Z. Zheng, *J. Mater. Chem. A* **2019**, *7*, 19662.

[39] Y. Yao, B. Kou, Y. Peng, Z. Wu, L. Li, S. Wang, X. Zhang, X. Liu, J. Luo, *Chem. Commun.* **2020**, *56*, 3206.

[40] Y. Hu, J. Schlipf, M. Wussler, M. L. Petrus, W. Jaegermann, T. Bein, P. Müller-Buschbaum, P. Docampo, *ACS Nano* **2016**, *10*, 5999.

[41] J. Schlipf, Y. Hu, S. Pratap, L. Bießmann, N. Hohn, L. Porcar, T. Bein, P. Docampo, P. Müller-Buschbaum, *ACS Appl. Energy Mater.* **2019**, *2*, 1011.

[42] Y. Liu, S. Akin, L. Pan, R. Uchida, N. Arora, J. V. Milić, A. Hinderhofer, F. Schreiber, A. R. Uhl, S. M. Zakeeruddin, A. Hagfeldt, M. I. Dar, M. Grätzel, *Sci. Adv.* **2019**, *5*, eaaw2543.

[43] D. Liang, C. Dong, L. Cai, Z. Su, J. Zang, C. Wang, X. Wang, Y. Zou, Y. Li, L. Chen, L. Zhang, Z. Hong, A. El-Shaer, Z.-K. Wang, X. Gao, B. Sun, *Small* **2021**, *17*, 2100972.

[44] R. Yang, R. Li, Y. Cao, Y. Wei, Y. Miao, W. L. Tan, X. Jiao, H. Chen, L. Zhang, Q. Chen, H. Zhang, W. Zou, Y. Wang, M. Yang, C. Yi, N. Wang, F. Gao, C. R. McNeill, T. Qin, J. Wang, W. Huang, *Adv. Mater.* **2018**, *30*, 1804771.

[45] T. Liu, J. Guo, D.i Lu, Z. Xu, Q. Fu, N. Zheng, Z. Xie, X. Wan, X. Zhang, Y. Liu, Y. Chen, *ACS Nano* **2021**, *15*, 7811.

[46] Y. Hu, L. M. Spies, D. Alonso-Álvarez, P. Mocherla, H. Jones, J. Hanisch, T. Bein, P. R. F. Barnes, P. Docampo, *J. Mater. Chem. A* **2018**, *6*, 22215.

[47] W. Yuan, G. Niu, Y. Xian, H. Wu, H. Wang, H. Yin, P. Liu, W. Li, J. Fan, *Adv. Funct. Mater.* **2019**, *29*, 1900234.

[48] X. Wang, K. Li, H. Xu, N. Ali, Y. Wang, Q. Shen, H. Wu, *Chem. Commun.* **2020**, *56*, 7917.

[49] F. Schmitz, J. Horn, N. Dengo, A. E. Sedykh, J. Becker, E. Maiworm, P. Bélteky, Á. Kukovecz, S. Gross, F. Lamberti, K. Müller-Buschbaum, D. Schlettwein, D. Meggiolaro, M. Righetto, T. Gatti, *Chem. Mater.* **2021**, *33*, 4688.

[50] E. R. Jette, F. Foote, *J. Chem. Phys.* **1935**, *3*, 605.

[51] K. Tvingstedt, O. Malinkiewicz, A. Baumann, C. Deibel, H. J. Snaith, V. Dyakonov, H. J. Bolink, *Sci. Rep.* **2014**, *4*, 6071.

[52] V. D'Innocenzo, G. Grancini, M. J. P. Alcocer, A. R. S. Kandada, S. D. Stranks, M. M. Lee, G. Lanzani, H. J. Snaith, A. Petrozza, *Nat. Commun.* **2014**, *5*, 3586.

[53] V. Sarritzu, N. Sestu, D. Marongiu, X. Chang, S. Masi, A. Rizzo, S. Colella, F. Quochi, M. Saba, A. Mura, G. Bongiovanni, *Sci. Rep.* **2017**, *7*, 44629.

[54] E. J. Juarez-Perez, M. Wußler, F. Fabregat-Santiago, K. Lakus-Wollny, E. Mankel, T. Mayer, W. Jaegermann, I. Mora-Sero, *J. Phys. Chem. Lett.* **2014**, *5*, 680.

[55] Y. Zhang, M. Liu, G. E. Eperon, T. C. Leijtens, D. McMeekin, M. Saliba, W. Zhang, M. de Bastiani, A. Petrozza, L. M. Herz, M. B. Johnston, H. Lin, H. J. Snaith, *Mater. Horiz.* **2015**, *2*, 315.

[56] W. Tress, M. Yavari, K. Domanski, P. Yadav, B. Niesen, J. P. Correa Baena, A. Hagfeldt, M. Graetzel, *Energy Environ. Sci.* **2018**, *11*, 151.

[57] P. Caprioglio, C. M. Wolff, O. J. Sandberg, A. Armin, B. Rech, S. Albrecht, D. Neher, M. Stolterfoht, *Adv. Energy Mater.* **2020**, *10*, 2000502.

[58] W. Tress, N. Marinova, O. Inganäs, M. K. Nazeeruddin, S. M. Zakeeruddin, M. Graetzel, *Adv. Energy Mater.* **2015**, *5*, 1400812.

[59] J. Jiménez-López, W. Cambarau, L. Cabau, E. Palomares, *Sci. Rep.* **2017**, *7*, 6101.

[60] P. J. Hasnip, K. Refson, M. I. J. Probert, J. R. Yates, S. J. Clark, C. J. Pickard, *Philos. Trans. A Math. Phys. Eng. Sci.* **2014**, *372*, 20130270.

[61] N. Giesbrecht, A. Weis, T. Bein, *J. Phys. Energy* **2020**, *2*, 024007.

[62] M. L. Petrus, K. Schutt, M. T. Sirtl, E. M. Hutter, A. C. Closs, J. M. Ball, J. C. Bijleveld, A. Petrozza, T. Bein, T. J. Dingemans, T. J. Savenije, H. Snaith, P. Docampo, *Adv. Energy Mater.* **2018**, *8*, 1801605.

[63] P. Giannozzi, S. Baroni, N. Bonini, M. Calandra, R. Car, C. Cavazzoni, D. Ceresoli, G. L. Chiarotti, M. Cococcioni, I. Dabo, A. Dal Corso, S. de Gironcoli, S. Fabris, G. Fratesi, R. Gebauer, U. Gerstmann, C. Gougoussis, A. Kokalj, M. Lazzeri, L. Martin-Samos, N. Marzari, F. Mauri, R. Mazzarello, S. Paolini, A. Pasquarello, L. Paulatto, C. Sbraccia, S. Scandolo, G. Sclauzero, A. P. Seitsonen, A. Smogunov, P. Umari, R. M. Wentzcovitch, *J. Phys. Condens. Mater.* **2009**, *21*, 395502.

[64] D. R. Hamann, *Phys. Rev. B* **2013**, *88*, 085117.

[65] P. Burke, Ernzerhof, *Phys. Rev. Lett.* **1996**, *77*, 3865.

[66] A. Tkatchenko, M. Scheffler, *Phys. Rev. Lett.* **2009**, *102*, 73005.

[67] R. L. Z. Hoye, P. Schulz, L. T. Schelhas, A. M. Holder, K. H. Stone, J. D. Perkins, D. Vigil-Fowler, S. Siol, D. O. Scanlon, A. Zakutayev, A. Walsh, I. C. Smith, B. C. Melot, R. C. Kurchin, Y. Wang, J. Shi, F. C. Marques, J. J. Berry, W. Tumas, S. Lany, V. Stevanović, M. F. Toney, T. Buonassisi, *Chem. Mater.* **2017**, *29*, 1964.

[68] T. Hellmann, C. Das, T. Abzieher, J. A. Schwenzer, M. Wussler, R. Dachauer, U. W. Paetzold, W. Jaegermann, T. Mayer, *Adv. Energy Mater.* **2020**, *10*, 2002129.